

Parametric Investigation on the Use of Lateral and Longitudinal Rotor Trim Flapping for Tiltrotor Noise Reduction

Carlos Malpica
Aerospace Engineer
NASA Ames Research Center
Moffett Field, CA

ABSTRACT

This paper presents an acoustics parametric study of the effect of varying lateral and longitudinal rotor trim flapping angles (tip-path-plane tilt) on noise radiated by an isolated 26-ft diameter proprotor, similar to that of the AW609 tiltrotor, in edgewise flight. Three tip-path-plane angle of attack operating conditions of -9 , 0 and 6 deg, at 80 knots, were investigated. Results showed that: 1) minimum noise was attained for the tip-path-plane angle of attack value of -9 deg, and 2) changing the cyclic trim state (i.e., controls) altered the airloads and produced noticeable changes to the low-frequency (LF) and blade-vortex interaction (BVI) radiated-noise magnitude and directionality. In particular, by trimming the rotor to a positive (inboard) lateral flapping angle of 4 deg, further reductions up to 3 dB in the low-frequency noise sound pressure level were attained without significantly impacting the BVI noise for longitudinal tip-path-plane angles of -9 and 6 deg.

NOTATION

a	speed of sound, ft/s or m/s
c	blade chord length, ft or m
C_n	blade section normal force coefficient
C_T	thrust coefficient
M	Mach number
M_x	Hub roll moment, ft-lb or Nm
M_y	Hub pitch moment, ft-lb or Nm
r	blade radial station
r_c	tip vortex core radius, ft or m
R	rotor radius, ft or m
α_{TPP}	tip path plane angle of attack, deg
α_s	shaft tilt angle, deg
β_{1c}	longitudinal blade flapping, deg
β_{1s}	lateral blade flapping, deg
μ	advance ratio
ρ	air density, slug/ft ³ or kg/m ³
σ	rotor solidity
θ_0	collective swashplate control, deg
θ_{1c}	lateral cyclic swashplate control, deg
θ_{1s}	longitudinal cyclic swashplate control, deg
ψ	rotor azimuth angle, rad or deg
BPF	Blade-Passage Frequency
BVI	Blade-Vortex Interaction
LF	Low-Frequency
SPL	Sound Pressure Level
TPP	Tip-Path-Plane
TRAM	Tilt Rotor Aeroacoustics Model

INTRODUCTION

The high levels of noise generated by helicopter operations remain at the heart of public opposition to the widespread use of rotorcraft for commercial transportation. Harmonic rotor noise is the major contributor of the noise generated by helicopters. There are, however, multiple mechanisms by which harmonic rotor noise is generated, and which are strongly dependent on the operating condition (Ref. 1). Because of the aural sensitivity of humans, and the separate mechanisms at play, it is natural to classify rotor noise as a function of the frequency range. Despite the subjective nature of noise perception by humans, low-frequency noise is typically considered one of the more obtrusive due to its larger propagation distance, in particular when impulsive in nature. Low-frequency noise from rotors, for example, can be the cause of vibration, or “rattling” of ground-based structures or facilities. Low-frequency in-plane noise, has been shown to have some dependency on the advancing blade aerodynamic loads. Blade-Vortex Interaction (BVI) is another objectionable source mechanism of rotor noise. BVI noise originates from the sharp impulsive blade loads that result from a rotor blade passing in close proximity to, or even striking, a blade tip vortex from the wake. BVI noise is a problem for civilian helicopter terminal area operations because it manifests itself primarily in descending flight, with peak noise occurring typically near standard 6-deg approach glideslopes.

Existing rotor noise attenuation techniques all aim to suppress the noise at the source, i.e., the aerodynamic forces on the blades. This can be achieved either through careful management or control of the approach flight path profile, or by means of active rotor control systems. Active rotor control, such as with Individual Blade Control (IBC), using

blade root-actuated systems in Ref. 2 and active flaps in the case of Ref. 3, operates by directly affecting the blade loading. These approaches have been shown to be somewhat effective in reducing both types of noise.

Other techniques for attenuating BVI noise rely on the management of the trim state of the rotor, primarily aiming to alter the tip-path-plane (TPP) angle of attack and wake geometry. One such technique is proposed in Ref. 4, where by varying the propulsive requirement on the rotor in trim (the X -force), the rotor plane must tilt proportionately in order to maintain vehicle equilibrium. This basic principle was at the heart of the research of Ref. 5, which showed that flying decelerating approaches could affect BVI noise by altering the rotor tip-path-plane angle of attack, which in turn altered the separation distance between the wake and the rotor. These same fundamental principles have also been successfully tested on the XV-15 tiltrotor (Ref. 6).

The combined effect of airframe drag and pitch moment effectors on BVI noise radiation of an S-70 helicopter in trim was studied in Refs. 7 and 8. The study in Ref. 7 confirmed that the primary mechanism for BVI noise reduction was achieved through the nose-down reorientation of the tip-path plane caused by increasing fuselage drag. In Ref. 8 it was argued that varying the rotor hub pitch moment, while keeping the tip-path-plane angle of attack constant, caused small changes in the wake and blade motions, which in turn resulted in slight changes in the maximum BVI noise radiated. Although these BVI noise changes could be characterized as being of a second-order nature, relative to the effect of airframe drag, the large effect on the fuselage pitch attitude, during trimmed flight, suggested that airframe pitch moment control could be used without significant penalty to the acoustics attenuation, to compensate for the uncomfortable change in fuselage pitch attitude introduced by a fuselage-mounted X -force BVI noise controller.

In the case of harmonic, low-frequency in-plane noise, reduction of the acoustic signature strength was achieved through the superposition of acoustic pulses generated by the blade airloads on the advancing side of the rotor in such a manner that attenuated the strong negative pressure peaks associated with the in-plane, steady thickness noise (Ref. 3). Because of the fundamental 1/rev characteristic of the blade loading, it was hypothesized herein that low-frequency noise reductions are attainable by modifying the lateral cyclic rotor trim control in such a manner that the modified airloads offset the steady thickness-related pressure peaks. Implementing this concept on a conventional single main rotor helicopter is difficult, however, because the side force and roll moment change would have to be counterbalanced by the airframe or tail rotor in order to maintain trim flight equilibrium with *tolerable* sideslip and roll attitude changes.

Tiltrotors represent intriguing rotorcraft configurations in the context of the present discussion. Not only does the unique reconfiguration capability of tiltrotors present an additional

degree of freedom for controlling the aerodynamic angle of attack of the rotor tip-path-plane (Ref. 9), aerodynamic drag and pitch moment control surfaces required for X -force control could be designed into the airframe with relative ease (Ref. 6). Also, through the application of differential lateral cyclic control, tiltrotors have the ability to offset the lateral forces and roll moments from both rotors, allowing the lateral cyclic of each rotor to be changed without affecting the trim flight equilibrium. Conceptually, differential (or symmetric) lateral cyclic control could be applied on a tiltrotor in trimmed flight, maintaining flight equilibrium, while effecting the 1/rev cyclic change in the airloads of both rotors required to attenuate the steady thickness noise.

In summary, the notion that altering the aerodynamic trim state of a rotorcraft main rotor will yield changes to its acoustic signature has been espoused. The need to maintain trim flight equilibrium, however, requires controlling the airframe aerodynamic loads in some fashion. This idea, in the form of the so-called X -force control, has been shown to be effective in attenuation of BVI noise. Inclusion of a pitch moment controller on the airframe to compensate for any potential attitude changes is key to make this a viable noise control technique, however. The hypothesis that low-frequency noise for a rotor in edgewise flight can be attenuated by changing the lateral cyclic trim control has also been introduced. Tiltrotors, over all other rotorcraft configurations, appear to be ideally suited to these noise attenuation concepts. The present hypothesis, that changes of 1/rev cyclic trim control can be used to attenuate negative pressure peak associated with the steady thickness noise, remains to be tested.

OBJECTIVE

The object of this parametric analysis is to investigate the sensitivity of low-frequency and BVI noise radiation of an isolated tiltrotor proprotor to changes in the lateral and longitudinal trim controls, under constant thrust and aerodynamic angle of attack settings.

TECHNICAL APPROACH

An isolated proprotor, similar to that of the AW609 tiltrotor, was chosen for this study. The AW609 is purported to be the first tiltrotor likely to enter service for civilian commercial transportation, which makes it a relevant subject of analysis. The AW609 rotor (Ref. 10) employs a gimballed hub. Its main characteristics are summarized in Table 1.

Table 1. AW609 Rotor Characteristics.

Characteristic	English	Metric
Number of blades	3	
Nominal rotor speed	569 rpm	
Rotor radius	13 ft	3.96 m
Tip speed	775 ft/s	236.3 m/s
Mean blade chord	1.233 ft	0.376 m
Rotor solidity (thrust-weighted)	0.09061	
Blade twist	47.5 deg	

Analysis Methodology

The methodology for deriving rotor noise predictions in this paper utilized a comprehensive rotor analysis, CAMRAD II (Ref. 11), and an acoustics analysis tool, PSU-WOPWOP (Ref. 12). CAMRAD II was first used to calculate trimmed rotor blade aeroelastic deflections and airloads. These were subsequently provided to PSU-WOPWOP, which computed acoustic pressures over a specified surface in space.

Comprehensive analysis. CAMRAD II models the blade structural properties, rotor wake geometry, and local unsteady blade aerodynamics. Within CAMRAD II, blade modeling is based on a series of span-wise distributed nonlinear beam finite elements. Each beam element is represented by a full range of blade motions, which includes axial, lead-lag, flapping and torsion. Specifically, the elastic deformation of the blade is characterized by the spatial displacements of any arbitrary point on the elastic axis and the Euler angle rotations of the blade cross-sections relative to a rotating blade frame of reference.

A non-uniform inflow model coupled to a free wake was used to obtain aerodynamic forces and blade motion solutions that satisfy the rotor thrust, propulsive force and pitch/roll moments required for the trim conditions. In all ensuing calculations, the rotor blade was modeled using 32 aerodynamic panels on each blade. The panels were more densely distributed near the tip of the rotor blade (at $0.025R$ intervals, outboard of the mid-span point), the dominant region important for sound radiation. Steady airloads were computed using C81 airfoil tables. Unsteady lift and moment in the attached flow were calculated based on compressible thin-airfoil theory.

For trim calculations, the aerodynamic loads on the blades were evaluated at azimuth intervals of 15 deg. The relatively large time (azimuth) step is adequate for capturing low frequency sound, but BVI noise calculation requires a time (azimuth) step of 1 deg or smaller, to capture higher frequency content. An azimuthal resolution of 1 deg was used in this study. CAMRAD II generates this fine azimuthal resolution after achieving a converged trim solution, by reconstructing the wake geometry and blade motion at the intermediate azimuths.

A dual-peak wake model of the tip vortex roll-up dynamics was used. Johnson (Ref. 13) suggested that the dual-peak model must be used because for operation in edgewise flight, at moderate speeds ($\mu = 0.125$ to 0.2), the high twist of the tiltrotor blades results in negative tip loading over most of the advancing side. In a dual-peak wake model the tip vortex is defined by the negative tip loading, and not by the maximum positive bound circulation on the inboard part of the blade, as is the case with the single-peak wake models conventionally used for analysis of helicopter rotors.

With a few exceptions, the key wake model features and parameters were set in consistence with the guidelines of

Ref. 13. For positive shaft angles (representing descent flight operation), reconstruction of the wake at 1 deg azimuth steps results in higher frequency BVI airloads over most of the advancing side, and to a lesser degree, on the retreating side. This behavior was amplified for smaller values of the tip vortex core radius. Therefore, as a compromise, a vortex core radius with a constant value of 80% mean chord ($r_c = 0.8c$) was used. Accordingly, the core radius of the inboard vortex (that models the rolled-up positive trailed vorticity inboard of the negative tip loading) was also scaled up to 120% mean chord. Two and four revolutions of wake were tried, with calculated free distortion. The more noticeable effect is for the rotors operating in descending conditions (positive shaft angle). Finally, the trailed vorticity was modelled to be partially entrained into the tip vortex after $1/4$ revolution of wake age, with the final tip vortex strength being equal to 70% of the peak bound circulation on the blade.

Normal force calculations from two wake models are compared in Figure 1 against measurements from a TRAM test at a similar condition. Here, exact agreement was not to be expected, but the comparison was useful to characterize

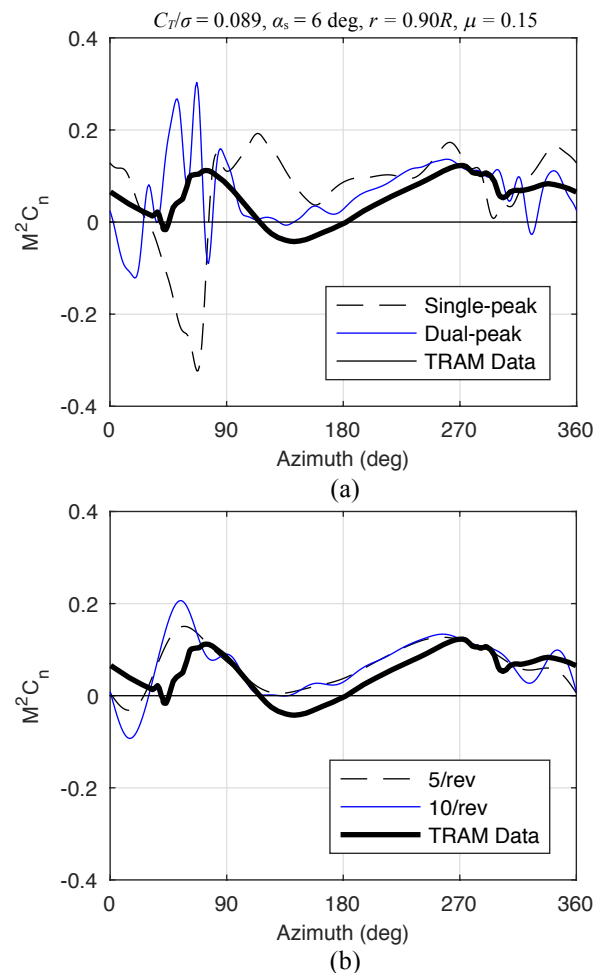


Figure 1. Calculated airloads: (a) total, (b) lowpass filtered dual-peak wake model

the general features of the airloads near the tip. The large region of negative loading over the advancing side that results from the single-peak wake model was evident in Figure 1a. Over-prediction of BVI airloads for the dual-peak model, even for a tip vortex core radius of 80% mean chord, was also evident in Figure 1a. Filtering the higher-frequency content by means of a lowpass filter (5 and 10/rev cut-off frequencies) revealed that the dual-peak wake model yielded an adequate characterization of the rotor blade airloads near the tip (Figure 1b).

Acoustics analysis. The acoustics prediction code, PSU-WOPWOP, uses the blade planform, airfoil geometry, and pre-determined aerodynamic loading to resolve rotor acoustics radiation in the time-domain, based on Farassat's Formulation 1A (Ref. 14). The noise is computed for any observer in both the near- and the far-field. For this study, PSU-WOPWOP was specifically configured to use the CAMRAD II computed blade motion and unsteady airloads.

Acoustic pressure time histories were computed over a notional 500-ft radius hemispherical grid of observers located below the rotor plane and centered at the rotor hub. These observers were spaced every 5 deg, and were aligned with the wind-tunnel (i.e., inertial) frame of reference, such that 0 deg elevation corresponds to the horizon, and cover the elevation range from 0 to -90 deg (the point directly below the hub), and a 360-deg azimuthal sweep. While the analysis was carried out for a single isolated rotor, and therefore only the effect of one rotor was calculated, it can be assumed that noise emission from a tiltrotor with two phase-locked rotors would be symmetric. For a complete acoustics analysis, the acoustic pressures from the symmetric rotor on the observer hemisphere would have to be mirrored and superposed to generate the total pressures.

Two sets of band-limited Sound Pressure Level (SPL) acoustic metrics were defined to isolate the low-frequency and BVI noise phenomena. The first set defined: 1) the Low-Frequency Sound Pressure Level (LFSPL), calculated by integrating the bandpass filtered sound pressure power between the 1st and 10th blade-passage frequency (BPF) harmonics (28.5–284.5 Hz), to focus on the low-frequency events; and 2) the BVI Sound Pressure Level (BVISPL), calculated from the filtered spectra between the 10th and 50th blade-passage harmonics (284.5–1422.5 Hz) to focus on the BVI events. The second set, LFSPL₂ and BVISPL₂, were calculated by filtering the sound pressure power between the 1st and 5th (142.2 Hz), and the 6th (170.7 Hz) and 50th blade-passage harmonics, respectively.

The operating environmental air density and temperature used in the analysis calculations were set to $\rho = 0.002378$ slug/ft (1.22557 kg/m³) and $T = 59$ °F (15 °C). These two conditions defined the speed of sound to be $a = 1116.45$ ft/s (340.3811 m/s).

Trim Procedure and Parametric Analysis Cases

Procedurally, the parametric investigation was conducted by independently varying the rotor lateral and longitudinal flapping trim target angles, while keeping a constant rotor thrust and tip-path-plane angle of attack. The trim controls were the collective and cyclic (lateral and longitudinal) swashplate inputs.

Results were for a single rotor in a wind tunnel trim, 80-knot airspeed condition, at a blade loading coefficient, C_T/σ , of 0.08. Three tip-path-plane angles of attack, α_{TPP} , of -9, 0 and 6 deg were analyzed. In practice, the tip-path-plane angles were achieved by setting the shaft tilt angle to these values, and trimming the rotor to zero 1/rev flapping ($\beta_{1c} = \beta_{1s} = 0$), defining, incidentally, the baseline trim conditions for the parametric analysis.

These three angles of attack were intended to cover a variety of operating conditions likely encountered by the rotor of a tiltrotor on approach to landing. Because of the additional nacelle angle reconfiguration degree of freedom, there is a wide range of angles of attack tiltrotor rotors can operate in, depending on flight path trajectory and pitch attitude. The rotor angle of attack of -9 deg was considered representative of the tiltrotor operating in a “nominal” 75-deg nacelle conversion configuration, and following a normal 3-deg glideslope on approach (assuming a 3 deg nose up pitch were maintained by the pilot). The 6 deg angle of attack condition was representative of a high BVI condition, and was analyzed to study the effect of lateral and longitudinal flapping in trim.

The tip-path-plane angle of attack is defined by the difference between the shaft tilt, α_s , and the longitudinal flapping, β_{1c} , the latter being defined as positive for a forward rotation of the rotor plane relative to the hub plane, such that:

$$\alpha_{TPP} = \alpha_s - \beta_{1c}. \quad (1)$$

The trim procedure was set to maintain a constant blade loading coefficient and tip-path-plane angle of attack, while varying the lateral and longitudinal rotor flapping angle trim targets. In order to ensure the constant tip-path-plane angle of attack when trimming to non-zero longitudinal flapping angle targets, the shaft tilt angle had to be adjusted in accordance with Eq. (1).

RESULTS

Effect of TPP Angle of Attack on BVI Noise

The calculated airloads, at 0.90R, shown in Figures 2 and 3 illustrate the increasing severity of the BVI events as the rotor plane tilts further aft. This is evident from dramatic increases in the amplitudes of the airloads pulses over the first quadrant on the advancing side of the rotor, and to a lesser degree at the fourth quadrant on the retreating side of the rotor. The calculated airloads, shown in Figure 3a, were

bandpass filtered between 10 and 50/rev, to isolate the effect of BVI-related airloads. The derivative of the normal force, shown in Figure 3b, further highlighted the impulsive nature of these BVI fluctuating airloads that ultimately manifest in BVI source noise generation.

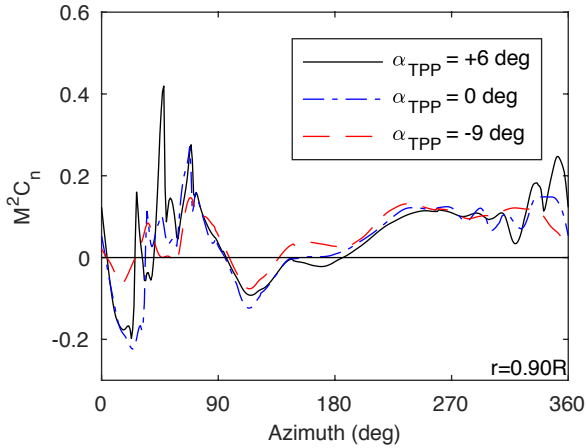


Figure 2. Calculated normal force for $\beta_{1c} = \beta_{1s} = 0$

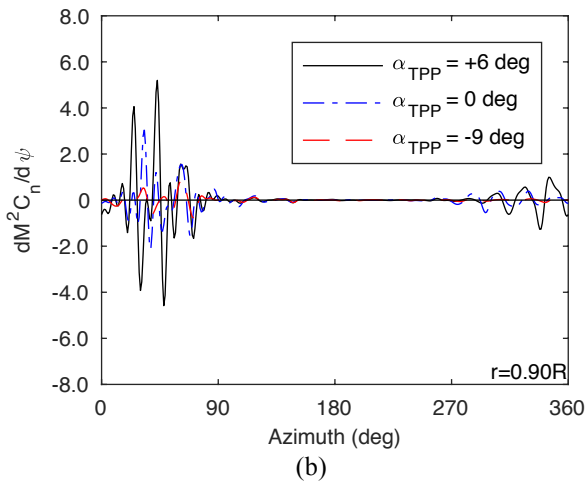
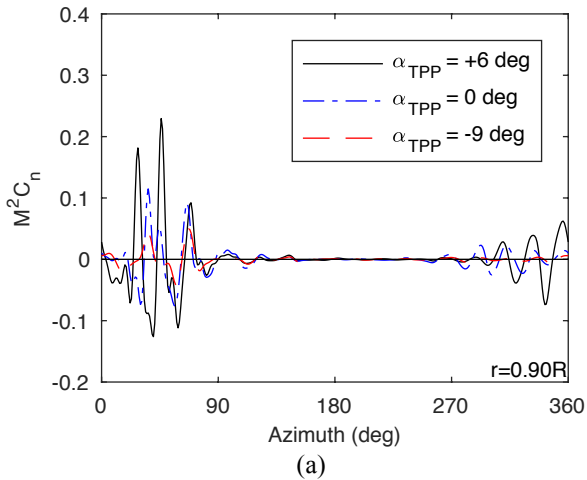


Figure 3. BVI bandpass filtered airloads for $\beta_{1c} = \beta_{1s} = 0$: (a) normal force, and (b) normal force derivative

The increasing trend of the BVISPL maximum calculated over the hemisphere from PSU-WOPWOP for these three conditions (Figure 4) mirrored this result. The nearly linear relationship between shaft angle and BVISPL maximum suggested these three conditions were on the upward slope of the BVISPL curve, and therefore the peak BVISPL for the given thrust condition should occur at some higher angle of attack ($\alpha_s = \alpha_{TPP} > 6$ deg).

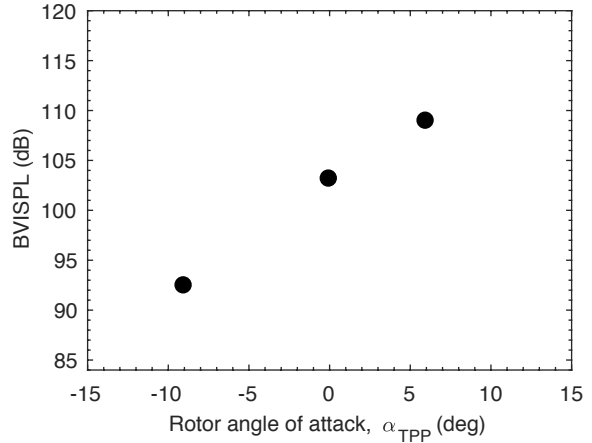


Figure 4. Calculated BVISPL maximum for $\beta_{1c} = \beta_{1s} = 0$

The strongest BVISPL (maximum) was shown in Figure 5 to be directed slightly forward of the advancing side, at an azimuth approximately between 90 and 130 deg, and an elevation between 25 and 60 deg below the horizon. This was greater than 108 dB for the 6 deg shaft tilt case, but only up to 92 dB for the nose down -9 deg shaft tilt. There was a slight change, between the two cases, in the directionality of the BVI noise radiated, however, with the lower shaft tilt radiating noise in a slightly more forward azimuth closer to 120-140 deg. The strong directionality of the BVI noise for the 6 deg shaft angle case was consistent with the location of the sharp normal force derivative peaks calculated at 25 and 43 deg azimuths. While there is a strong dependency of BVI noise directionality on the interaction angle and the trace Mach number (Refs. 15-17), and these were not ascertained herein, it is common for BVI events to occur at these azimuths. Typically, the earlier the BVI occurs, the more it is directed toward the advancing side. Likewise, one should expect the interactions to occur earlier as the TPP angle of attack increases, since the part of the wake intersecting the rotor plane commonly moves aft.

Effect of Rotor Flapping on BVI Noise

Calculated BVISPL values in Figure 6 illustrate the second-order nature of the effect of varying the longitudinal tip-path-plane tilt, at constant angle of attack, with only slight increases in the BVISPL maximum for the off-baseline conditions. Overall, the baseline case resulted in the lowest BVI acoustic signature of the five cases. Incidentally, this result was found to be consistent with the findings of Ref. 8.

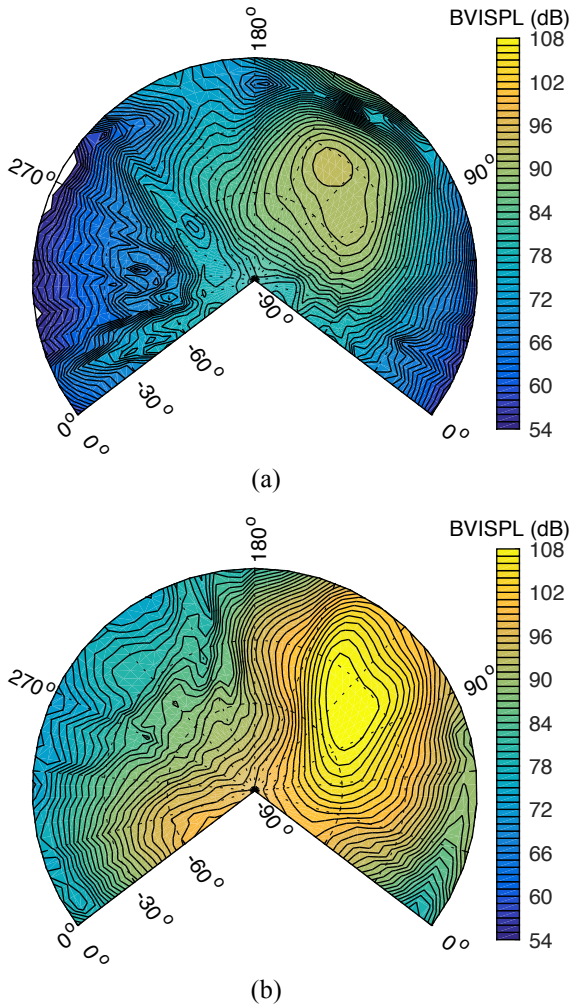


Figure 5. Calculated BVISPL contours: (a) $\alpha_{\text{TPP}} = -9$ deg, (b) $\alpha_{\text{TPP}} = 6$ deg

For $\beta_{1c} = 4$ deg, the maximum BVISPL was approximately 1.9 dB larger than the baseline condition. The stronger BVI condition was also evident from the larger hotspot roughly between 90 and 130 deg azimuth, and elevations between -20 and -65 deg (Figure 7). The largest BVISPL increase occurs near the 210 deg azimuth, but absolute BVISPL in this direction is initially low. Ultimately, the approximate 2 dB increase of BVI noise maximum over large regions on the advancing side was attributed to relatively stronger BVI events occurring near the aft region of the rotor, and which were evidenced by the bandpass filtered normal force derivative peaks between 345 and 15 deg (Figure 8). The dominant peaks were still found near 25 and 41 deg azimuths, and these were the primary cause of the strong BVI radiated in the 90-130 deg azimuthal range. These results suggest changes in the directionality of the BVI noise were negligible, with the region defined by the 108-dB contour line being consistently constrained to azimuthal angles in the range from 90 to 130 deg.

Variations of the lateral flapping (tip-path-plane tilt) angle resulted in even smaller changes to the maximum BVISPL,

with an increase of less than 1 dB in the maximum BVISPL for $\beta_{1s} = -4$ deg. The change in the maximum BVISPL for $\beta_{1s} = 4$ deg was effectively negligible.

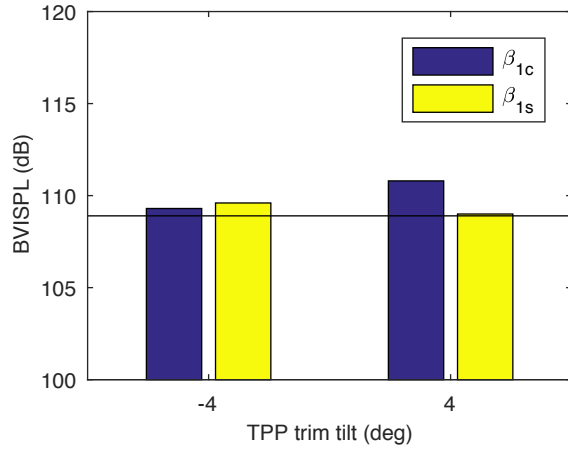


Figure 6. Calculated BVISPL maximum for $\alpha_{\text{TPP}} = 6$ deg

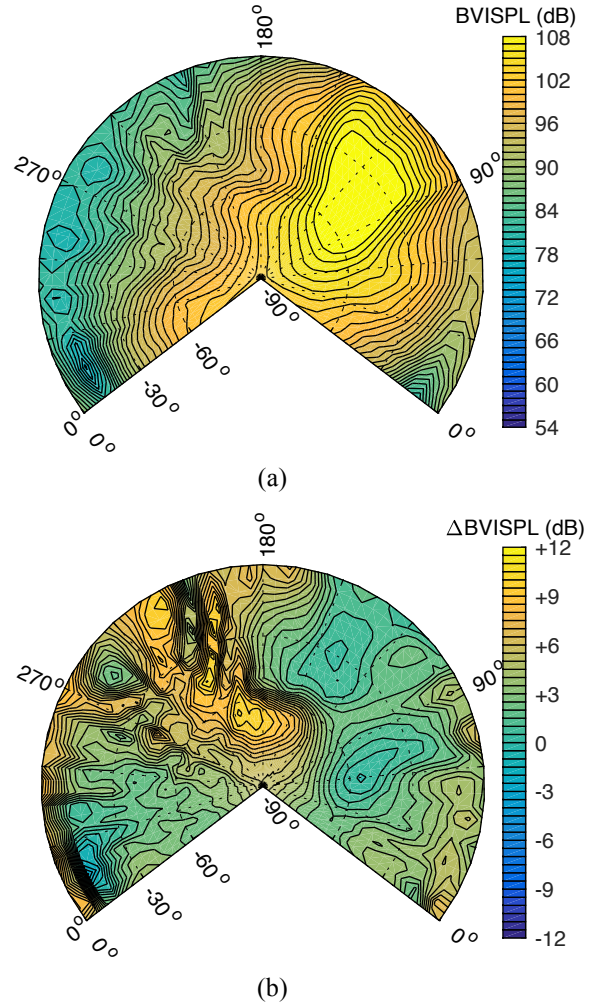


Figure 7. Calculated BVISPL contours for $\alpha_s = 6$ deg and $\beta_{1c} = 4$ deg: (a) absolute, and (b) difference with respect to $\beta_{1c} = 0$ deg

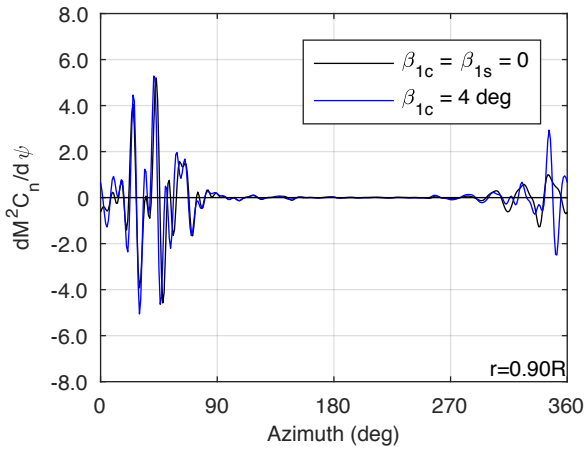


Figure 8. BVI bandpass filtered normal force derivative for $\alpha_s = 6$ deg

Effect of TPP Angle of Attack on Low-Frequency Noise

The LFSPL contours calculated for shaft angles of -9 , 0 and 6 deg in Figure 9 show the general effect of the TPP angle of attack on the radiated low-frequency noise. Note that the TPP angle of attack, α_{TPP} , and shaft tilt angle, α_s , are used interchangeably throughout the ensuing discussion because the rotor was trimmed to zero longitudinal flapping ($\beta_{1c} = 0$).

Overall, a shaft tilt angle (as proxy to a TPP angle of attack) of -9 deg was the more favorable operating condition in terms of both the BVISPL and LFSPL of the radiated noise. Interestingly, results tended to track the BVI results, with peak LFSPL increasing as a function of shaft angle (or, equivalently, TPP angle of attack). Generally, low-frequency noise also tended to be radiated in the same direction as BVI noise, at approximate azimuth and elevation angles of 100 and -45 deg, respectively, for the higher shaft angles (0 and 6 deg). This result is likely due to the definition of the LFSPL including more BVI harmonics than expected.

Recall that the observer hemisphere was aligned with the inertial frame. Therefore, some of the LFSPL directionality changes in Figure 9 were due to the shaft angle (or TPP) reorientation, with the 6 deg shaft angle configuration clearly radiating more out-of-plane noise forwards at a 0 deg elevation angle (the horizon).

Figure 10 illustrates the normal force derivative at 90% span location for the three tip-path-plane angles. The larger peak-to-peak values for 0 - and 6 -deg tip-path-plane angles were consistent with the higher LFSPL values in Figure 9. As with the BVI airloads shown in the previous sections, the normal force, of which derivatives are shown in Figure 10 (and subsequent Figures), were bandpass filtered (between 1 and $10/\text{rev}$) to isolate the low-frequency effects.

Acoustic pressure time histories for an observer at azimuth and elevation angles of 100 and -45 deg, respectively, are shown in Figure 11. For this observer position, out-of-plane loading was confirmed to be a major source of the LFSPL.

Accordingly, thickness noise contributions were negligible. Note that pressure signals in Figure 11 were bandpass filtered between 1 and 10 BPF to allow comparison with the airloads. The increasing peak-to-peak amplitudes of the acoustic pressures with respect to the shaft angle were consistent with the normal force derivative peak-to-peak

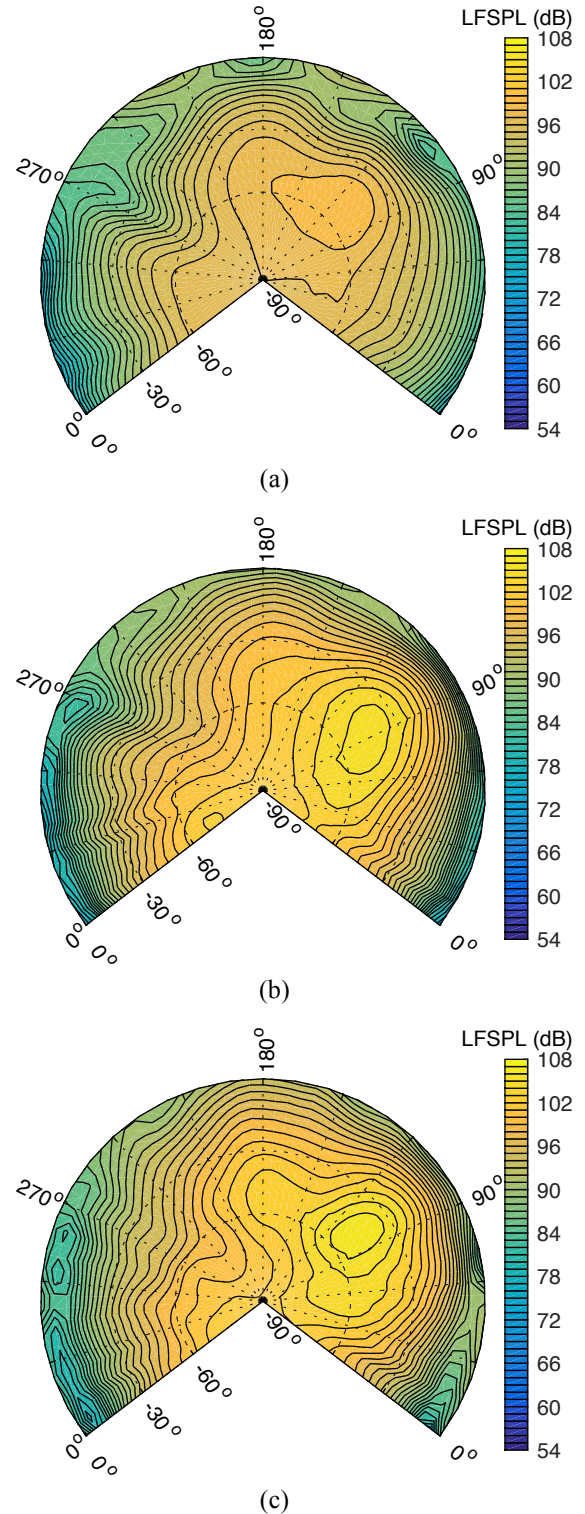


Figure 9. Calculated LFSPL contours: (a) $\alpha_s = -9$ deg, (b) $\alpha_s = 0$ deg, and (c) $\alpha_s = 6$ deg

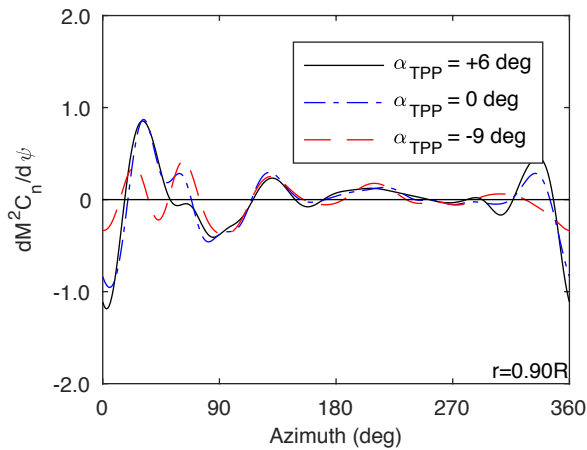


Figure 10. Low-frequency bandpass filtered normal force derivative for $\beta_{1c} = \beta_{1s} = 0$

amplitudes of Figure 10. Peaks and minima in the acoustic pressures were effectively traced one-to-one to the normal force derivative topography for $\alpha_s = -9$ deg and $\alpha_s = 0$ deg. This same relationship was not as obvious for $\alpha_s = 6$ deg.

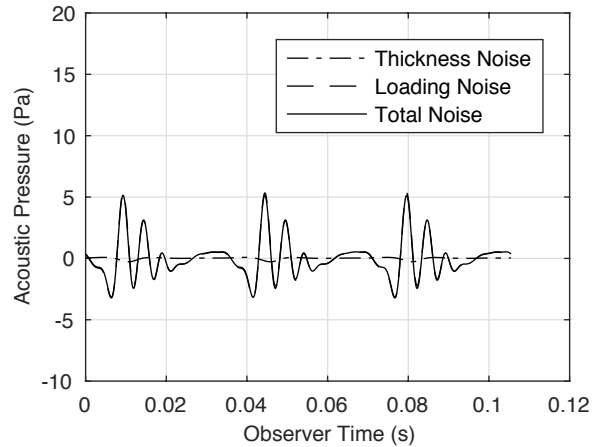
Effect of Lateral Flapping on Low-Frequency Noise

The trim lateral flapping, β_{1s} , was found to have differing effects on low-frequency noise, depending on tip-path-plane angle. This is illustrated in Figures 12–17. Trimming the rotor to a negative lateral flapping of -4 deg, for example, had a very different effect on the LFSPL for a rotor at a tip-path-plane angle of -9 deg (Figure 12a), 0 deg (Figure 14a) or 6 deg (Figure 16a).

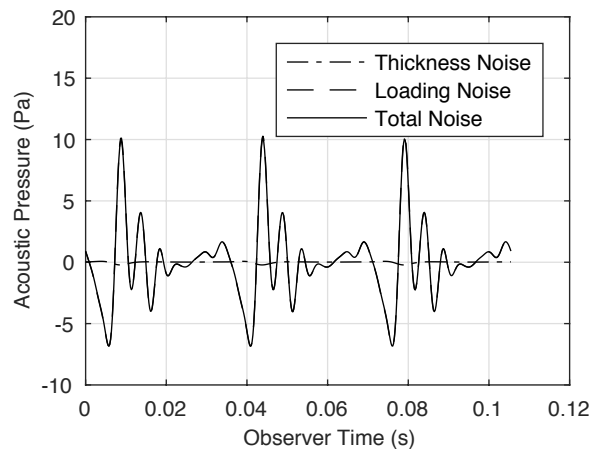
LFSPL contours in Figure 12 illustrate the low-frequency noise effect of changing the trim lateral flapping for a (longitudinal) shaft (or tip-path-plane) angle of -9 deg. The LFSPL was increased by nearly 6 dB, in a direction forward of 90 deg (Figure 12a), via trimming the rotor to a negative (outboard) lateral tilt ($\beta_{1s} = -4$ deg). This LFSPL increase was focused at an elevation angle of approximately 10 deg below the horizon. The overall region of increased LFSPL spanned the azimuth range from 30 to 270 deg, with the largest increases directed over the advancing side, between 30 and 180 deg. Within this region, however, there was also a reduction of the LFSPL over a frontal arc spanning an azimuthal range between 120 and 180 deg, at an elevation which suggests it to be a reduction of the in-plane noise. This increase in LFSPL values on the observer hemisphere was consistent with the peak-to-peak amplitude of the normal force derivative, which increased significantly near the 45 deg blade azimuth compared to the baseline condition (Figure 13).

A very different result was observed for a positive (inboard) β_{1s} of 4 deg, where the low-frequency noise was reduced by up to 3 dB over a broad region of the observer hemispherical surface (Figure 12b). The largest reduction was directed toward the direction of the advancing blade ($\psi = 90$ deg).

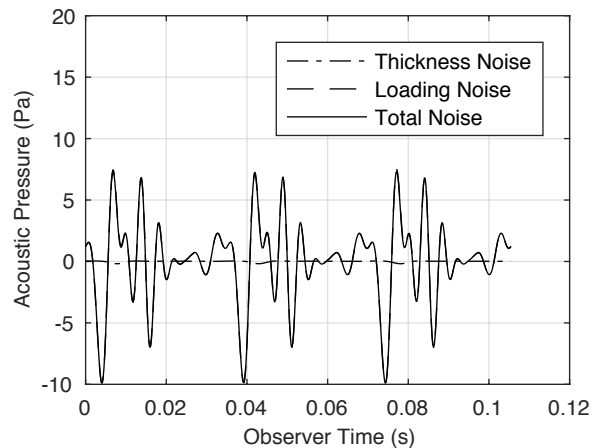
This general reduction was attributed to smaller normal force derivatives (Figure 13).



(a)



(b)



(c)

Figure 11. Low-frequency bandpass filtered acoustic pressure time histories for observer at azimuth 100 deg and elevation -45 deg: (a) $\alpha_s = -9$ deg, (b) $\alpha_s = 0$ deg, and (c) $\alpha_s = 6$ deg

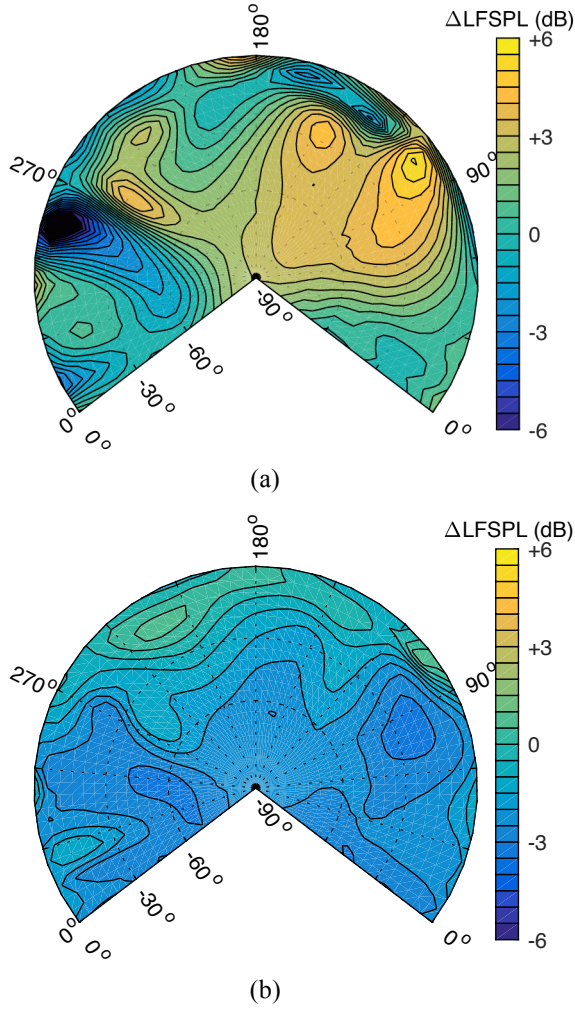


Figure 12. Calculated Δ LFSPL contours for $\alpha_s = -9$ deg: (a) $\beta_{1s} = -4$ deg, and (b) $\beta_{1s} = 4$ deg

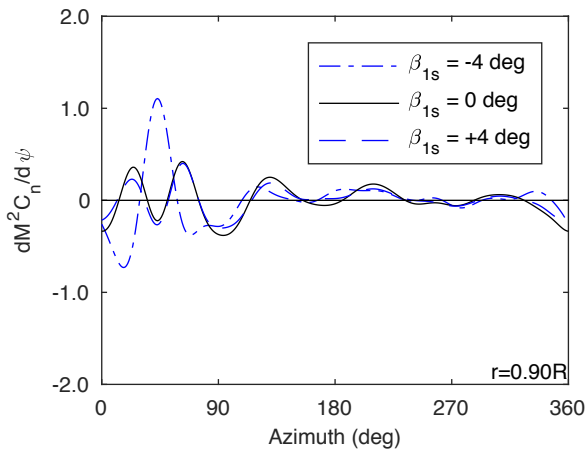


Figure 13. Low-frequency bandpass filtered normal force derivative for $\alpha_s = -9$ deg

Qualitatively, with the rotor operating in a pure edgewise flight condition, with $\alpha_s = 0$ deg, the effect of trimming to positive or negative β_{1s} appeared to have minimal effects on the LFSPL (Figure 14). The negative case ($\beta_{1s} = -4$ deg) tended to slightly redirect low-frequency noise more forward and towards higher (smaller) elevation angles, compared to the positive ($\beta_{1s} = 4$ deg) case. This effect was correlated with the slight phasing difference of the dominant normal force derivative peak observed over the advancing side in both cases (Figure 15).

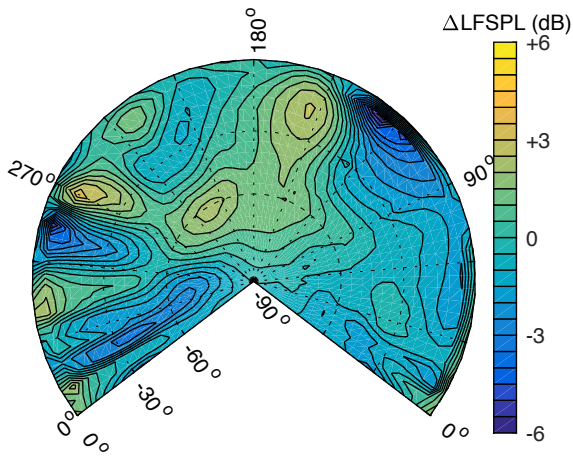
At a tip-path-plane angle of attack of 6 deg, the negative β_{1s} trim resulted in relatively small changes to the LFSPL (Figure 16a). The only noticeable change in the normal force derivative was found in the peak-to-peak amplitude over the retreating side of the rotor, near the aft position (Figure 17). The apparent effect on the LFSPL seemed to be concentrated towards the horizon and within an azimuth range of 0 to 80 deg.

In contrast, a positive β_{1s} trim resulted in LFSPL reductions in directions both aft and forward of the advancing blade (Figure 16b), which combined with a slight increase in an azimuthal direction of 80 deg, had the overall effect of directing the LFSPL peak more narrowly in the direction of the advancing blade. These regions of reduced LFSPL were consistent with the significantly reduced peak-to-peak amplitude of the normal force derivative (Figure 17).

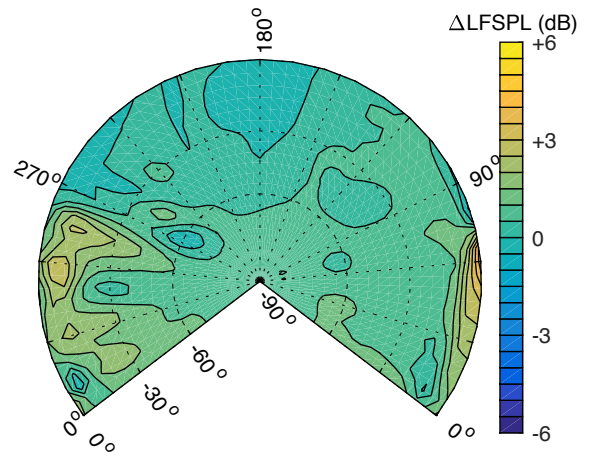
While changes in the lateral trim flapping angle resulted in noticeable effects on the LFSPL distribution over the observer hemisphere, many of these LFSPL differences were localized and did not translate into significant changes of the LFSPL maximums. LFSPL maximums for the nine trim conditions are shown in Table 2. For a shaft angle of -9 deg, the maximum LFSPL increased by 3.4 dB for a *negative* lateral flapping angle of -4 deg and decreased by 1.8 dB for a *positive* lateral flapping angle of 4 deg. For higher shaft angle configurations (0 and 6 deg), varying the lateral trim flapping angle resulted in minimal changes to the maximum LFSPL. The largest Δ LFSPL observed for these cases was on the order of 0.4 dB (for $\alpha_s = 6$ deg and $\beta_{1s} = 4$ deg).

Table 2. LFSPL Maximums (dB)

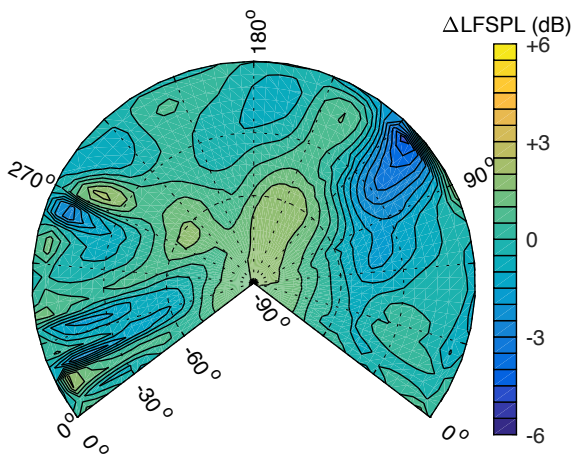
Shaft angle (deg)	Lateral flapping angle (deg)		
	-4	0	4
-9	102.3	98.9	97.1
0	104.5	104.4	104.3
6	106.0	105.7	106.1



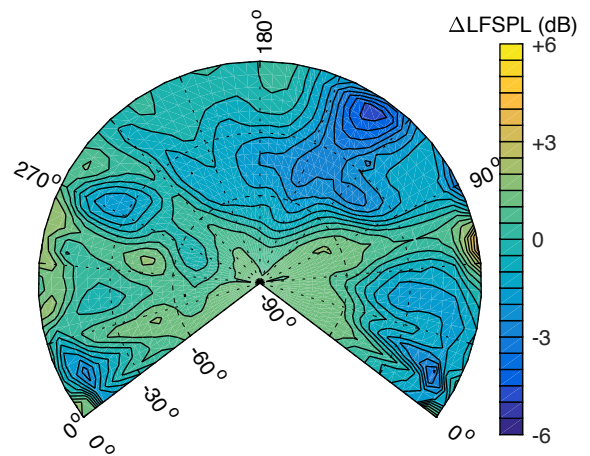
(a)



(a)



(b)



(b)

Figure 14. Calculated Δ LFSPL contours for $\alpha_s = 0$ deg:
 (a) $\beta_{1s} = -4$ deg, and (b) $\beta_{1s} = 4$ deg

Figure 16. Calculated Δ LFSPL contours for $\alpha_s = 6$ deg:
 (a) $\beta_{1s} = -4$ deg, and (b) $\beta_{1s} = 4$ deg

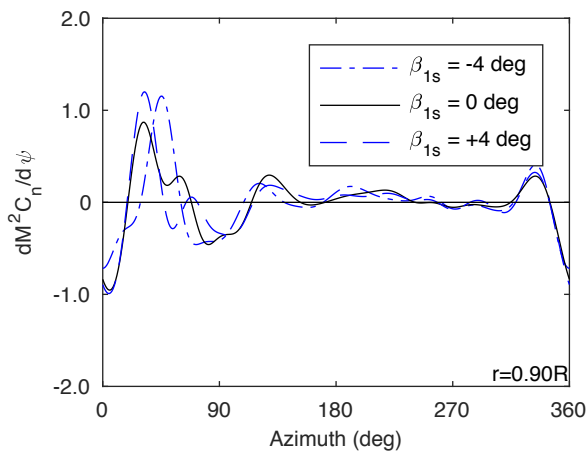


Figure 15. Low-frequency bandpass filtered normal force derivative for $\alpha_s = 0$ deg

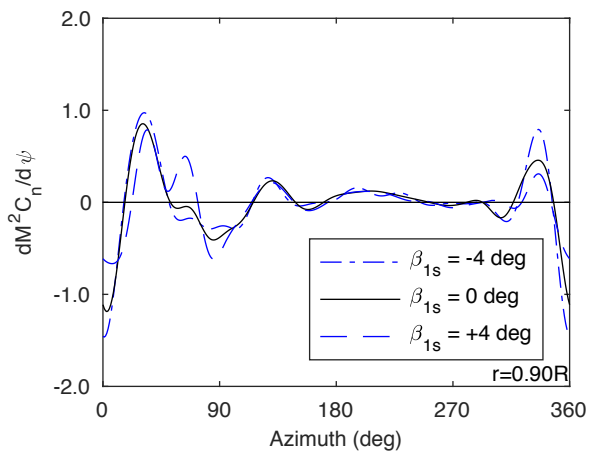


Figure 17. Low-frequency bandpass filtered normal force derivative for $\alpha_s = 6$ deg

LFSP₂ and BVISPL₂ Characterization

Baseline analysis. Results for BVI (Figure 5) and low-frequency (Figure 9) noise suggest the LFSP₂ definition, allowing harmonics up to the 10th BPF (284.5 Hz), included more BVI harmonics than expected. LFSP₂ and BVISPL₂ contours, shown in Figure 18, illustrate clearly distinct characteristics between low-frequency and BVI noise when separated by a 142.2 Hz threshold. Both metrics had a maximum value near 97.6 dB, but possessed distinct differences in their directionality. LFSP₂ was directed forwards and down (at a -50 deg elevation), directly over the path of the rotor. The BVISPL₂ was directed towards an azimuth of 105 deg and an elevation of -45 deg. One further aspect of the SPL₂ predictions was that LFSP₂ was overall lower magnitude than LFSP, and BVISPL₂ higher than BVISPL.

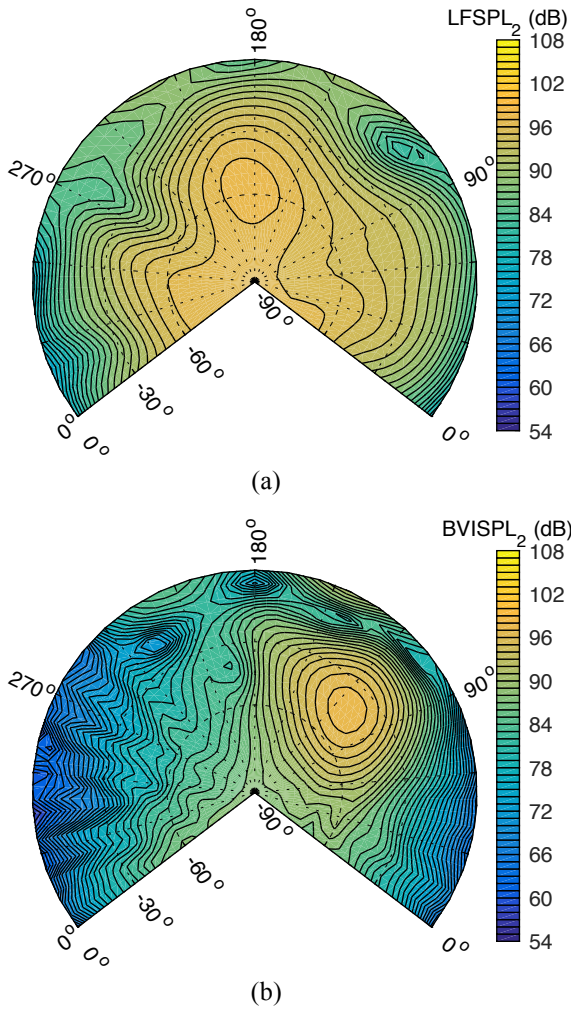


Figure 18. Calculated Sound Pressure Level contours for $\alpha_s = -9$ deg: (a) LFSP₂ and (b) BVISPL₂

Comparison of the BVISPL₂ and LFSP₂ contours for a 6-deg shaft angle (Figure 19) also illustrate broad increases in the BVI and reductions in the low-frequency sound pressure level metrics, relative to BVISPL (Figure 5b) and LFSP (Figure 9c) calculations.

This was to be expected, because harmonics in the 6-9 BPF range were removed from the integration of the sound pressure power spectra in the calculation of LFSP₂ and included into the BVISPL₂ calculation. Thus, LFSP₂ maximums for the baseline trim cases ($\beta_{1s} = 0$ deg) shown in Table 3 decreased by 1.3 to 4.2 dB, relative to the LFSP maximums for the same condition. The LFSP₂ values for shaft angles of 0 and 6 deg showed the largest reductions, on account of the airloads calculations for these trim points predicting (possibly even over-predicting) larger amplitude BVI loads.

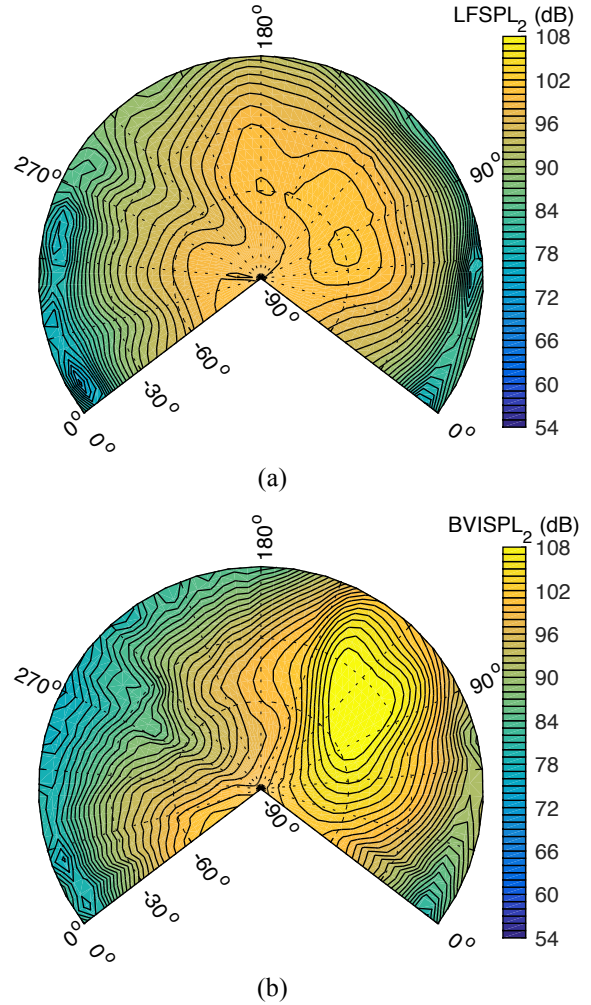


Figure 19. Calculated Sound Pressure Level contours for $\alpha_s = 6$ deg: (a) LFSP₂ and (b) BVISPL₂

Table 3. LFSP₂ Maximums (dB)

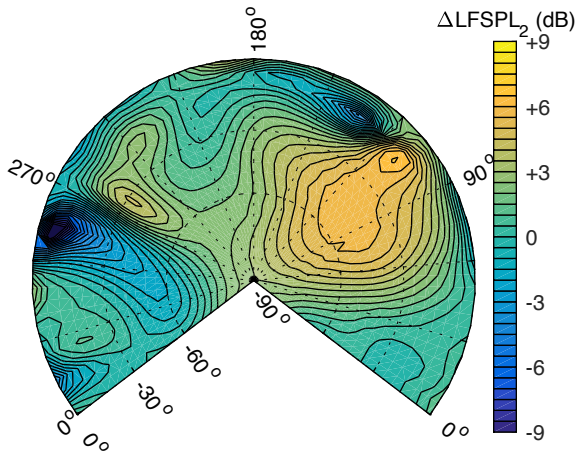
Shaft angle (deg)	Lateral flapping angle (deg)		
	-4	0	4
-9	101.0	97.6	95.4
0	100.9	102.0	101.2
6	102.7	101.5	98.6

Parametric analysis. The effect of lateral trim flapping on LFSPL₂ maximums is also summarized in Table 3. The pure edgewise flow condition ($\alpha_s = 0$ deg) excepted, 2 to 3 dB reductions in the maximum LFSPL₂ were obtained for a positive lateral flapping ($\beta_{1s} = 4$ deg). For $\beta_{1s} = -4$ deg, however, a significant increase (3.4 dB) in maximum LFSPL₂ was obtained for a shaft angle of -9 deg, only. Results for $\alpha_s = 0$ deg were generally insensitive to lateral flapping changes, with the largest differences being on the order of ~ 1 dB; a result, incidentally, consistent with LFSPL predictions in Table 2.

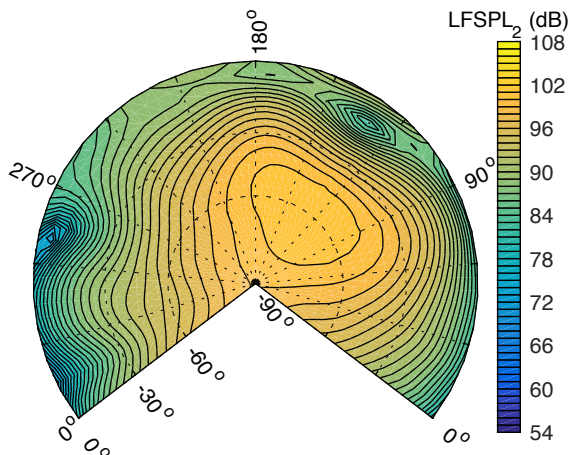
LFSPL₂ contours shown in Figure 20, for $\beta_{1s} = -4$ deg, and Figure 21, for $\beta_{1s} = 4$ deg, follow the same trend as that for LFSPL (Figure 12). Trimming to a negative flapping angle of 4 deg, the LFSPL₂ calculations showed in Figure 20a a 6.6 dB increase directed towards an azimuth of 110 deg and an elevation of -15 deg. This was only a slight change in directionality compared to LFSPL contours in Figure 12a. In general, the LFSPL₂ increases spanned the same broad

region, spanning azimuth angles from 30 to 270 deg. Similarly, the frontal arc between 120 and 210 deg, also exhibited a reduction along an elevation corresponding to the location of the rotor plane projection on the observer hemisphere. Figure 20b shows the effect of these LFSPL₂ changes on the absolute value, clearly expanding the region that is subjected to the high levels of low-frequency noise. Maximum LFSPL₂ was close to 101 dB, a 3.4 dB increase over the baseline ($\beta_{1s} = 0$ deg).

Whereas the negative flapping angle caused the low-frequency noise to increase, trimming to a positive lateral flapping of 4 deg had the opposite effect, in a similar way to that on the LFSPL shown in Figure 12b. The maximum reduction of the LFSPL₂ was in the order of 5 dB (Figure 21a), with reductions occurring over a broad region of the observer hemisphere. The only LFSPL₂ increases (up to 2 dB) were found over a frontal arc associated with the in-plane rotor noise. The effect on the absolute LFSPL₂ is shown Figure 21b, indicating a 2.2 dB reduction in the LFSPL₂ maximum.

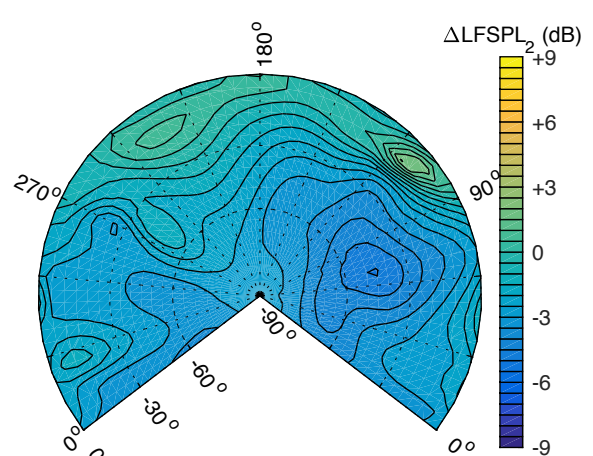


(a)

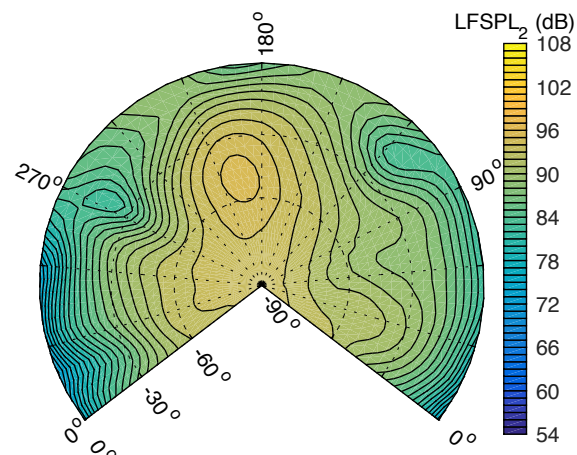


(b)

Figure 20. Calculated LFSPL₂ contours for $\alpha_s = -9$ deg and $\beta_{1s} = -4$ deg: (a) difference with respect to $\beta_{1s} = 0$ deg and (b) absolute



(a)



(b)

Figure 21. Calculated LFSPL₂ contours for $\alpha_s = -9$ deg and $\beta_{1s} = 4$ deg: (a) difference with respect to $\beta_{1s} = 0$ deg and (b) absolute

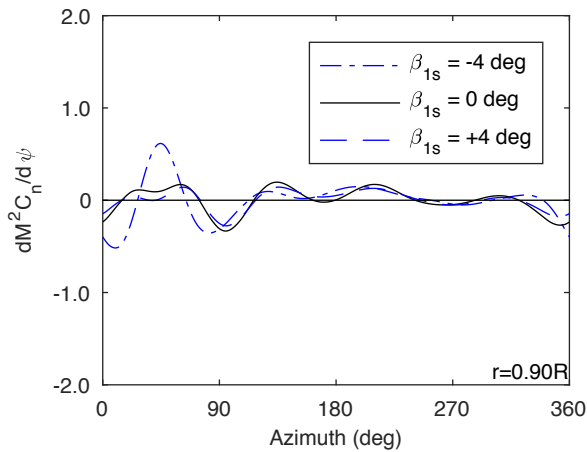
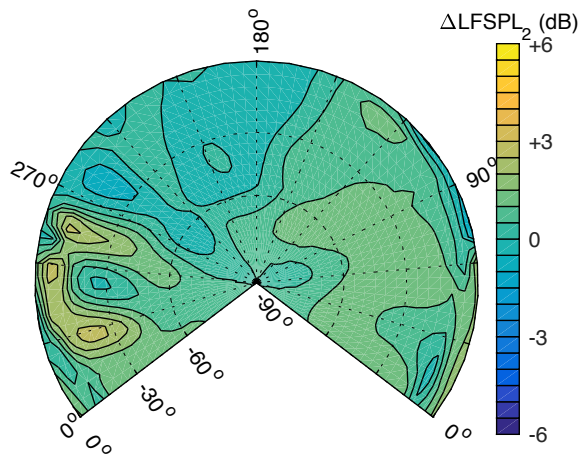
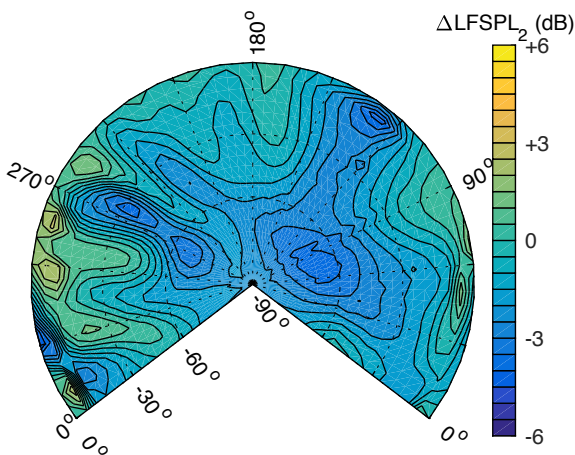


Figure 22. Low-frequency bandpass filtered (1-5/rev) normal force derivative for $\alpha_s = -9$ deg



BSN04: SPL difference in the range: -0.93, 2.67.

(a)



BSP04: SPL difference in the range: -4.58, 2.23

(b)

Figure 23. Calculated ΔLFSPL_2 contours for $\alpha_s = 6$ deg: (a) $\beta_{1s} = -4$ deg and (b) $\beta_{1s} = 4$ deg

The similarity in the trends is confirmed by the azimuth derivatives of the bandpass filtered normal force (Figure 22), which compare favorably with those from Figure 13. To reflect the same relationship between the SPL metric, the calculated normal forces used to compute the derivatives in Figure 22 were filtered between the 1st and the 5th /rev harmonics.

The LFSPL₂ differences, shown in Figure 23, displayed general similarities with the results for LFSPL shown in Figure 16. The main differences were found for trim at a positive (4 deg) flapping angle (Figures 23b and 16b). Elimination of the BVI harmonics from the LFSPL₂ definition resulted in a larger, more defined, region of LFSPL₂ reduction over the observer hemisphere. A local 3.7 dB minimum in the ΔLFSPL_2 was predicted over an azimuth spanning 60 to 90 deg, and a steep elevation, at 60 deg below the horizon plane. This location was exactly at the spot where the LFSPL₂ maximum was located (Figure 19a), suggesting the change in β_{1s} had a direct effect on the airloads causing the LFSPL₂ maximum.

A Brief Note on Rotor Trim

Rotor cyclic and collective controls required for trim at the various shaft angles of attack ($\alpha_s = -9, 0$ and 6 deg) and lateral flapping trim targets ($\beta_{1s} = -4, 0$ and 4 deg) are shown in Figure 24. The amplitude of the collective pitch was found to decrease for increasing lateral flapping trim targets. Conversely, the cyclic pitch controls increased as function of the lateral flapping trim targets. Lateral cyclic, θ_{lc} , was negative for $\beta_{1s} = -4$ deg and increased linearly, reversing sign for β_{1s} between -4 and 0 deg, and reaching its maximum value for $\beta_{1s} = 4$ deg. The rotor hub roll moment, M_x , increased accordingly (Figure 25) at an approximate rate of 100 ft-lb/deg of β_{1s} , with absolute changes on the order of 900 ft-lb, from minimums on the order of -300 ft-lb up to maximums of 600 ft-lb.

Trim hub moment results in Figure 25 showed non-trivial changes in the off-axis pitch moment, M_y , in particular for a shaft angle of -9 deg. For free flight trim, these pitch moment variations would need to be counteracted by aerodynamic control surfaces on the airframe to maintain trim equilibrium at a *constant* pitch attitude. Herein, the longitudinal flapping angle trim target was systematically set to zero ($\beta_{1c} = 0$ deg) to ensure constant tip-path-plane angle of attack while the lateral flapping angle, β_{1s} , was varied. An alternative approach would have been to trim the rotor to zero hub pitch moment, but this would have resulted in non-zero changes of the tip-path-plane angle of attack, with ensuing changes in the propulsive equilibrium and correlated acoustic effects. Ultimately, whichever approach were taken, maintaining trim equilibrium while adjusting the trim setting on the rotor for noise reduction requires the adjustment of aerodynamic forces and moments on the airframe. This role would fall on the automatic flight control system.

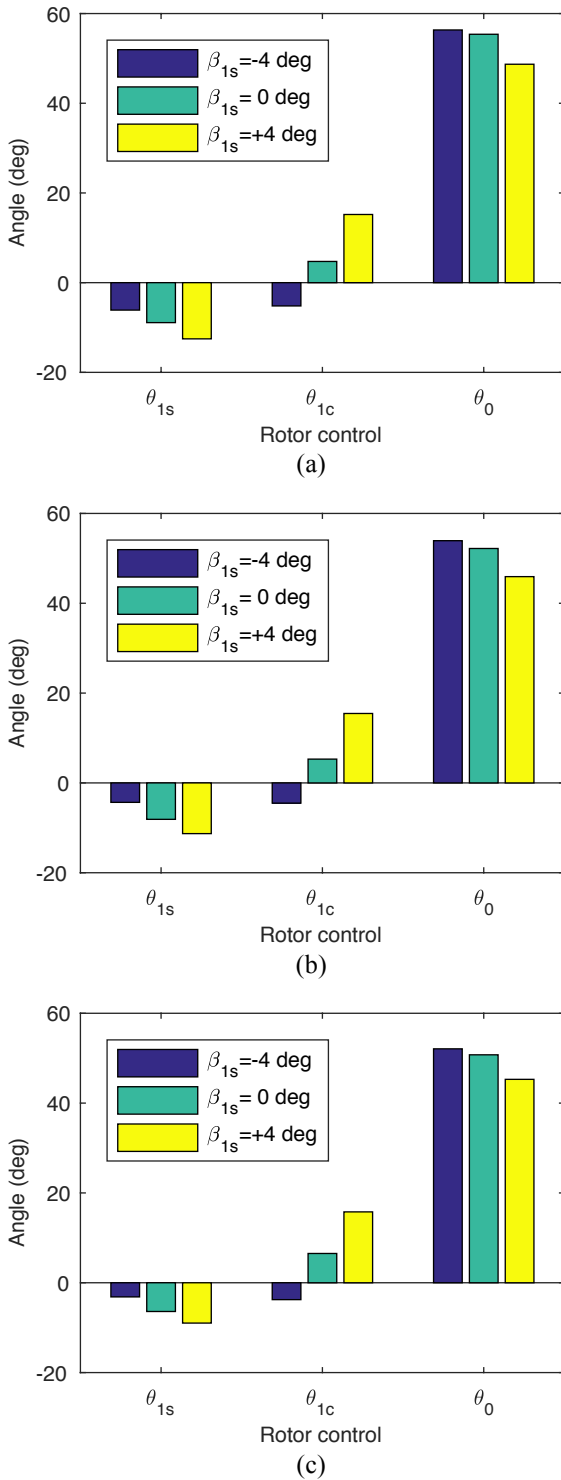


Figure 24. Calculated rotor trim controls: (a) $\alpha_s = -9$ deg, (b) $\alpha_s = 0$ deg, and (c) $\alpha_s = 6$ deg

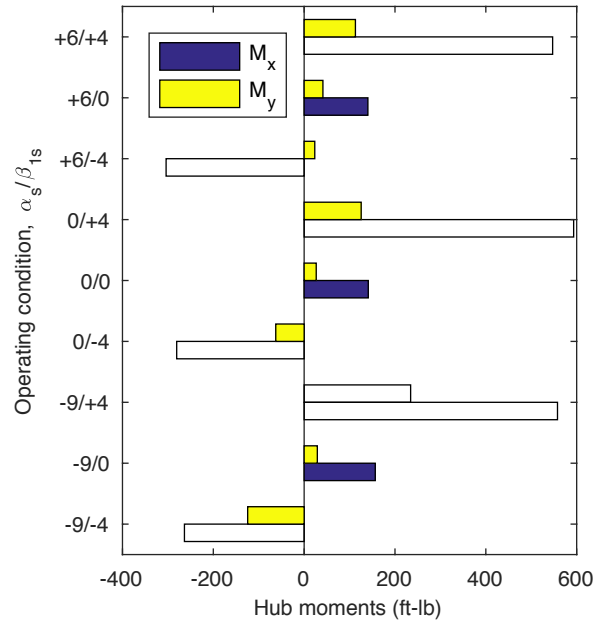


Figure 25. Calculated trim hub moments

CONCLUSIONS

Based on the results presented in this paper, the following conclusions were established:

1. Varying the angle of attack of the rotor caused large changes in the amplitude of the advancing blade aerodynamic loads but small changes in their phasing, which led to large increases in the magnitude of BVISPL and LFSPL, but minimal changes in their directionality.
2. Defined by a higher cut-off frequency of 142.2 Hz, LFSPL₂ was less sensitive to BVI airloads, when compared to LFSPL (284.5 Hz cut-off).
3. The effect of changes in the trim lateral flapping on the airloads and radiated-noise depended strongly on the angle of attack operating condition.
4. A shaft angle of -9 deg resulted in smallest normal force gradients over the advancing blade, and thus resulted in the lowest BVI and low-frequency noise radiated.
5. Trimming the rotor at shaft angles of -9 and 6 deg, with an inboard tilt ($\beta_{1s} = 4$ deg) yielded up to 3 dB reductions in the LFSPL₂ maximum value.

REFERENCES

¹Schmitz, F. H., "Rotor Noise," *Aeroacoustics of Flight Vehicles, Theory and Practice, Vol. 1: Noise Sources*, Ch. 2., Published for the Acoustical Society of America through the American Institute of Physics, 1995.

²Jacklin, S. A. et al., "Full-Scale Wind Tunnel Test of an Individual Blade Control System for a UH-60

- Helicopter," American Helicopter Society 58th Annual Forum, Montreal, Canada, June 11-13, 2002.
- ³Sim, B. W., JanakiRam, R. D., and Lau, B. H., "Reduced In-Plane, Low Frequency Noise of an Active Flap Rotor," American Helicopter Society 65th Annual Forum, Grapevine, TX, May 27-29, 2009.
- ⁴Schmitz, F. H., "Reduction of Blade-Vortex Interaction (BVI) Noise Through X-Force Control," NASA TM-110371, September 1995.
- ⁵Schmitz, F. H., Gopalan, G., and Sim, B. WC., "Flight-Path Management/Control Methodology to Reduce Helicopter Blade-Vortex Interaction Noise," *Journal of Aircraft*, Vol. 39, (2), March-April 2002, pp. 193-205.
- ⁶Conner, D. A., Edwards, B. D., Decker, W. A., Marcolini, M. A., and Klein, P. D., "NASA/Army/Bell XV-15 Tiltrotor Low Noise Terminal Area Operations Flight Research Program," *Journal of the American Helicopter Society*, Vol. 47, (4), October 2002, pp. 219-232.
- ⁷Malpica, C., Greenwood, E., and Sim, B., "Helicopter Non-Unique Trim Strategies for Blade-Vortex Interaction (BVI) Noise Reduction," Presented at the AHS Technical Meeting on Aeromechanics Design for Vertical Lift, San Francisco, CA, January 20-22, 2016.
- ⁸Malpica, C. A., Greenwood, E., and Sim, B. W., "Parametric Investigation of the Effect of Hub Pitching Moment on Blade Vortex Interaction (BVI) Noise of an Isolated Rotor," Presented at the AHS 72nd Annual Forum, West Palm Beach, FL, May 17-19, 2016.
- ⁹Gervais, M., "Tiltrotor Noise Reduction through Flight Trajectory Management and Aircraft Configuration Control," Ph.D. Dissertation, Department of Aerospace Engineering, University of Maryland, College Park, MD, 2004.
- ¹⁰Crane, D., Sherrill, P., Measom, R., and Miller, M., "Enabling Technology for the BA609 Proprotor Blade," Presented at the American Helicopter Society 61st Annual Forum, Grapevine, TX, June 1-3, 2005.
- ¹¹Johnson, W., "Rotorcraft Aerodynamics Models for a Comprehensive Analysis," American Helicopter Society 54th Annual Forum, Washington, DC, May 20-22, 1998.
- ¹²Shirey, J. S., Brentner, K. S., and Chen, Hn., "A Validation Study of the PSU-WOPWOP Rotor Noise Prediction System," 45th AIAA Aerospace Sciences Meeting and Exhibit, Reno, NV, January 8-11, 2007.
- ¹³Johnson, W., "Influence of Wake Models on Calculated Tiltrotor Aerodynamics," American Helicopter Society Aerodynamics, Acoustics, and Test and Evaluation Technical Specialists Meeting, San Francisco, CA, January 23-25, 2002.
- ¹⁴Farassat, F., "Derivation of Formulations 1 and 1A of Farassat," NASA/TM-2007-214853, March 2007.
- ¹⁵Lowson, M. V., "Directionality of Helicopter BVI Noise," 21st European Rotorcraft Forum, Saint-Petersburg, Russia, August 30 - September 1, 1995.
- ¹⁶Schmitz, F. H. and Sim, B. W., "Radiation and Directionality Characteristics of Helicopter Blade-Vortex Interaction Noise," *Journal of the American Helicopter Society*, Vol. 48, (4), October 2003, pp. 253-269.
- ¹⁷Leishman, G. J., *Principles of Helicopter Aerodynamics*, 2nd ed., Cambridge University Press, New York, NY, United States of America.
- ¹⁸Greenwood, E., Schmitz, F. H., and Sickenberger, R. D., "A Semi-Empirical Noise Modeling Method for Helicopter Maneuvering Flight Operations," American Helicopter Society 68th Annual Forum, Ft. Worth, TX, May 2012.
- ¹⁹van der Wall, B. G., "The Effect of HHC on the Vortex Convection in the Wake of a Helicopter Rotor," *Aerospace Science and Technology*, Vol. 4, (5), 2000, pp. 321-336.
- ²⁰Beddoes, T. S., "Practical Computation of Unsteady Lift," *Vertica*, Vol. 8, (1), 1984.
- ²¹Beddoes, T. S., "A Wake Model for High Resolution Airloads," International Conference on Rotorcraft Basic Research, February 1985.
- ²²Leverton, J. W., "Helicopter Noise: What is the Problem?," *VERTIFLITE*, Vol. 60, No. 2, March/April 2014, pp. 12-15.